

# Massive Dirac quasinormal modes in Schwarzschild–de Sitter black holes: Anomalous decay rate and fine structure

Almendra Aragón,<sup>1,\*</sup> Ramón Bécar,<sup>2,†</sup> P. A. González,<sup>1,‡</sup> and Yerko Vásquez<sup>3,§</sup>

<sup>1</sup>*Facultad de Ingeniería y Ciencias, Universidad Diego Portales,  
Avenida Ejército Libertador 441, Casilla 298-V, Santiago, Chile*

<sup>2</sup>*Departamento de Ciencias Matemáticas y Físicas, Universidad Católica de Temuco,  
Montt 56, Casilla 15-D, Temuco, Chile*

<sup>3</sup>*Departamento de Física, Facultad de Ciencias, Universidad de La Serena,  
Avenida Cisternas 1200, La Serena, Chile*



(Received 13 October 2020; accepted 9 February 2021; published 2 March 2021)

Recently, the anomalous decay rate of quasinormal modes has been studied for some geometries under scalar field perturbations, which occurs when the longest-lived modes are the ones with higher angular number, as well as the existence of a critical scalar field mass, i.e., the value of scalar field mass such that the decay rate does not depend appreciably on the angular number, and beyond which the behavior of the decay rate is inverted. Here, we consider the propagation of fermionic fields in the background of Schwarzschild–de Sitter black holes, and we show that the anomalous decay rate behavior and the fine structure, related to the coupling between the chirality and the mass of the field, can be observed in the fermionic spectrum.

DOI: [10.1103/PhysRevD.103.064006](https://doi.org/10.1103/PhysRevD.103.064006)

## I. INTRODUCTION

Quasinormal modes (QNMs) and the frequencies of QNMs or quasinormal frequencies (QNFs) have been a subject of study for a long time [1–5] and have recently acquired great interest due to the detection of gravitational waves [6,7]. The QNMs of different spin fields on Schwarzschild, Schwarzschild–de Sitter and Schwarzschild–anti–de Sitter spacetimes have been studied extensively, with the scalar field the most studied case. Considering the scenario when the black hole is immersed in an expanding universe, the QNMs of black holes in de Sitter (dS) space result of interest. However, due to the observed value of the cosmological constant is very small, it would be reasonable to ask why we should not neglect its effects in local physics, or more precisely, how strong are its perturbative effects. Also, from a modern point of view, the study of the dynamical properties of dS black holes provides important insight into de Sitter/conformal field theory correspondence (dS/CFT) [8–10]. Thus, following these interesting issues it is natural to study the propagation of test field in dS spacetimes.

The gravitational QNMs of Schwarzschild–de Sitter black hole were studied in Ref. [11] by following a procedure analogous to that of Chandrasekhar [12], and based on the Wentzel-Kramers-Brillouin (WKB) approximation in

Ref. [13]. Then, the existence of exponentially decaying tails at late times was demonstrated in Ref. [14] and the dynamics of radiative fields was analyzed in Ref. [15]. After that, via an analytical expression for the QNMs and QNFs of nearly extreme Schwarzschild–de Sitter black holes, it was demonstrated that the Pöschl-Teller is the true potential [16], in good agreement with those found by Moos *et al.* [17]. Other analytical approximation to the problem of scalar field perturbation on Schwarzschild–de Sitter black holes was studied, and it was shown the presence of two sets of modes relevant at two different timescales, proportional to the surface gravity of the black hole and to the cosmological horizon, respectively [18]. As well, the QNMs were calculated by using the sixth order WKB formula and the approximation by the Pöschl-Teller potential, and it was shown that the QNFs all have a negative imaginary part, which means that the propagation of scalar field is stable in this background, and the presence of the cosmological constant leads to decrease of the frequency of oscillation and to a slower decay rate [19]. Further, high overtones of gravitational and electromagnetic QNMs were studied in Ref. [20]. Also, an exhaustive analysis was performed by considering the WKB approach and two numerical schemes: the characteristic and general initial value integrations [21]. Additionally, a simple derivation of the imaginary parts of the QNFs was proposed by calculating the scattering amplitude in the first Born approximation and determining its poles [22]. Later, the QNMs of massless scalar field was studied for a Reissner-Nordström de Sitter (RNdS) black hole with a global monopole by the 6th order WKB approximation, and

\* almendra.aragon@mail.udp.cl

† rbecar@uct.cl

‡ pablo.gonzalez@udp.cl

§ yvasquez@userena.cl

it was discussed in detail how the parameters of black hole space-time influence the QNMs of massless scalar field [23]. Also, the phenomenon of slowly decaying resonances for Schwarzschild–de Sitter spacetimes, in the large scalar mass approximation was studied in Ref. [24]. Besides, it was found a novel infinite set of purely imaginary modes, which depending on the black hole mass may even be the dominant mode [25], and the different families of modes were recently study in detail in Ref. [26], and the different families of massless scalar fields in the exterior of RNdS black holes were analyzed in Ref. [27]. Finally, very recently it was investigated the relaxation rate of the  $d$ -dimensional RNdS black hole perturbed by neutral massless scalar field in the eikonal limit [28], finding that fastest rate relaxation increases with the cosmological constant for all dimensions, in addition it was analyzed the relationship between the cosmological constant and the critical charge and their influence on relaxation rate of the composed system.

On the other hand, it was recently shown that the decay rate of scalar QNMs in Schwarzschild, Schwarzschild–de Sitter, and Schwarzschild–AdS black holes present an anomalous behavior, i.e., the longest-lived modes are the ones with higher angular number, while that for Schwarzschild and Schwarzschild–de Sitter there is a critical scalar field mass, such that beyond this value the anomalous decay rate behavior is inverted [26,29]. Also, such anomalous behavior was shown for black holes in  $f(R)$  gravity [30], Reissner-Nordström black holes [31], and accelerating black holes [32].

Having in mind that the studies of anomalous decay rate have been performed for scalar perturbations, in this work, we study the propagation of massive fermionic fields in Schwarzschild–de Sitter black hole backgrounds, in order to see if the anomalous decay rate behavior and a critical fermionic field mass are present in the spectrum, as well as the fine structure. We carry out this study by using the pseudo-spectral Chebyshev method [33] which is an effective method to find high overtone modes [34–38]. It is worth mentioning that the study of the QNMs of the Dirac field has been performed for massless fermionic fields [19,39,40] and massive fermionic fields [41]. The results show that the field with higher masses and larger cosmological constant will decay more slowly in a Schwarzschild–de Sitter black hole by using the WKB approximation [41]. Also, the Dirac QNMs of  $D$ -dimensional de Sitter spacetime was determined in Ref. [42]. On the other hand, it was shown that the two chiralities of massive fermions lead to an additional fine structure in the spectrum, for Schwarzschild and Kerr backgrounds by using the convergent Frobenius method [43].

The manuscript is organized as follows: In Sec. II, we give a brief review of the spacetime that we have considered, and we study the Dirac equation. Then, in Sec. III, we calculate the QNFs of massless and massive fermionic fields numerically by using the pseudospectral Chebyshev method, and for massive fields we study the fine structure and the anomalous decay rate. Finally, we conclude in Sec. IV.

## II. FERMIONIC PERTURBATIONS

The Schwarzschild–de Sitter black holes are solutions of the equations of motion that arise from the Einstein-Hilbert action with a positive cosmological constant

$$S = \frac{1}{16\pi G} \int d^4x \sqrt{-g} (R - 2\Lambda), \quad (1)$$

where  $G$  is the Newton constant,  $R$  is the Ricci scalar, and  $\Lambda$  is the cosmological constant. The Schwarzschild–de Sitter black hole is described by the metric

$$ds^2 = f(r)dt^2 - \frac{dr^2}{f(r)} - r^2 d\Omega^2, \quad (2)$$

where  $d\Omega^2 = d\theta^2 + \sin^2\theta d\phi^2$ ,  $f(r) = 1 - \frac{2M}{r} - \frac{\Lambda r^2}{3}$ ,  $M$  is the black hole mass, and  $\Lambda > 0$ . This metric represents a black hole when  $\Lambda < 1/(9M^2)$ , with two horizons: the event horizon  $r_H$  and the cosmological horizon  $r_\Lambda$ , where  $r_H < r_\Lambda$ , and for  $\Lambda = 1/(9M^2)$  both horizons coincide.

In order to study the propagation of fermionic fields in the background of Schwarzschild–de Sitter black holes we consider the Dirac equation in curved space given by

$$(\gamma^\mu \nabla_\mu + m)\psi = 0, \quad (3)$$

where the covariant derivative is defined as  $\nabla_\mu = \partial_\mu + \frac{1}{2}\omega^{ab}{}_\mu J_{ab}$ , with  $\omega^{ab}$  being the Levi-Civita spin connection and  $J_{ab} = \frac{1}{4}[\gamma_a, \gamma_b]$  correspond to the generators of the Lorentz group, which are defined through the gamma matrices in a flat spacetime  $\gamma^a$ , that can be expressed through the gamma matrices in curved space-time  $\gamma^\mu$  by  $\gamma^\mu = e^\mu{}_a \gamma^a$ . So, in order to solve the Dirac equation (3), we use the diagonal vielbein

$$\begin{aligned} e^0 &= \sqrt{f} dt, & e^1 &= \frac{1}{\sqrt{f}} dr, \\ e^2 &= r d\theta, & e^3 &= r \sin\theta d\phi, \end{aligned} \quad (4)$$

and from the null torsion condition  $de^a + \omega^a{}_b \wedge e^b = 0$ , we obtain the nonzero components of the spin connection

$$\begin{aligned} \omega^{01} &= \frac{f'(r)}{2} dt, & \omega^{12} &= -\sqrt{f} d\theta, \\ \omega^{13} &= -\sqrt{f} \sin\theta d\phi, & \omega^{23} &= -\cos\theta d\phi. \end{aligned} \quad (5)$$

Now, using the following representation of the gamma matrices [44,45]  $\gamma^0 = i\sigma^2 \otimes \mathbf{1}$ ,  $\gamma^1 = \sigma^1 \otimes \mathbf{1}$ ,  $\gamma^m = \sigma^3 \otimes \tilde{\gamma}^m$ , where  $\sigma^i$  are the Pauli matrices, and  $\tilde{\gamma}^m$  are the Dirac matrices in the base manifold  $\Omega$ , along with the following ansatz for the fermionic field

$$\psi = \frac{e^{-i\omega t}}{r f^{1/4}} \begin{pmatrix} \psi_1 \\ \psi_2 \end{pmatrix} \otimes \varsigma, \quad (6)$$

where  $\psi_1$  and  $\psi_2$  are functions of  $r$  and  $\varsigma(\theta, \phi)$  is a 2-components fermion, we obtain the following equations:

$$-\frac{i\omega}{\sqrt{f}}\psi_2 + \sqrt{f}\psi_2' + \frac{i\kappa}{r}\psi_1 + m\psi_1 = 0, \quad \frac{i\omega}{\sqrt{f}}\psi_1 + \sqrt{f}\psi_1' - \frac{i\kappa}{r}\psi_2 + m\psi_2 = 0, \quad (7)$$

where  $i\kappa$  is the eigenvalue of the Dirac operator on the two-dimensional sphere, and  $\kappa$  can take positive and negative integer values  $\kappa = \pm(\ell + 1)$ , with  $\ell = 0, 1, 2, \dots$ , and the prime denotes the derivative with respect to the radial coordinate  $r$ . These equations can be decoupled as

$$\psi_1'' + \left( \frac{1}{2} \frac{f'(r)}{f(r)} + \frac{i\kappa}{r(i\kappa - mr)} \right) \psi_1' + \frac{r^2\omega(mr - i\kappa)(2\omega - if'(r)) - 2f(r)((i\kappa + mr)(i\kappa - mr)^2 - \kappa r\omega)}{2r^2 f(r)^2 (mr - i\kappa)} \psi_1 = 0, \quad (8)$$

$$\psi_2'' + \left( \frac{1}{2} \frac{f'(r)}{f(r)} + \frac{i\kappa}{r(i\kappa + mr)} \right) \psi_2' + \frac{r^2\omega(mr + i\kappa)(2\omega + if'(r)) - 2f(r)((-i\kappa + mr)(i\kappa + mr)^2 - \kappa r\omega)}{2r^2 f(r)^2 (mr + i\kappa)} \psi_2 = 0. \quad (9)$$

Notice that Eq. (9) can be obtained from Eq. (8) by means of the substitutions  $\psi_1 \rightarrow \psi_2$ ,  $\omega \rightarrow -\omega$  and  $\kappa \rightarrow -\kappa$ . On the other hand, the above equations (7), for a massless fermionic field, can be reduced to

$$-i\omega Z_+ - \frac{dZ_+}{dr^*} = WZ_+, \quad (10)$$

$$-i\omega Z_- - \frac{dZ_-}{dr^*} = -WZ_-, \quad (11)$$

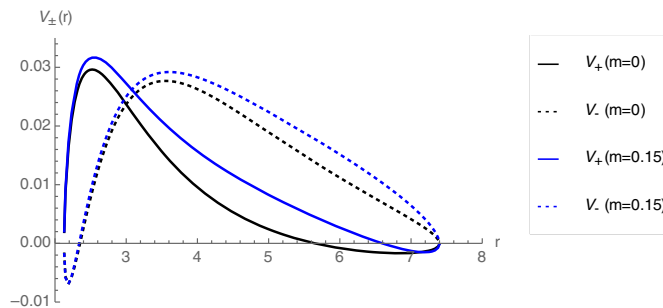
where we have defined  $Z_{\pm} = \psi_1 \pm i\psi_2$  and  $W = -i\kappa\sqrt{f}/r$ ; see Ref. [12], and the tortoise coordinate  $r^*$  is defined as usual by  $dr^* = dr/f$ . Now, decoupling Eqs. (10) and (11), we obtain the following Schrödinger-like equations:

$$-\frac{d^2 Z_{\pm}}{dr^{*2}} + V_{\pm} = \omega^2 Z_{\pm}, \quad (12)$$

where the effective potentials  $V_{\pm}$  are given by

$$V_{\pm} = W^2 \pm \frac{dW}{dr^*} = \mp \kappa \frac{f\sqrt{f}}{r^2} \pm \kappa \frac{f'\sqrt{f}}{2r} + \frac{\kappa^2 f}{r^2}. \quad (13)$$

We can observe that the potentials are not positive definite. Also it is possible to demonstrate that the effective potentials for massive fermionic field are



$$V_{\pm} = W^2 \pm \frac{dW}{dr^*}, \quad (14)$$

where

$$W[r] = \frac{\sqrt{f(r)}\sqrt{m^2 + \frac{\kappa^2}{r^2}}}{1 + \frac{1}{2\omega} f(r) \left( \frac{m\kappa}{m^2 r^2 + \kappa^2} \right)}. \quad (15)$$

The behavior of the effective potentials as a function of  $r$  is shown in Fig. 1 for a low value of the parameter  $\kappa = 1$ , with  $M = 1$ ,  $\Lambda = 0.04$  (left panel) and  $\Lambda = 0.11$  (right panel), and for a higher value of  $\kappa = 30$  in Fig. 2, with  $M = 1$ , and  $\Lambda = 0.11$ . The effective potentials of Fig. 1 exhibit negative gaps,  $V_-$  has a negative gap around the neighborhood of the event horizon, while that  $V_+$  has a negative gap around the cosmological horizon. Usually when the effective potential is negative in some region, growing perturbations can appear in the spectrum indicating an instability of the system under such perturbations. However in Ref. [39] the authors studied the stability of the massless Dirac field on Schwarzschild–de Sitter black holes via time-domain integration of the scalar wave equation finding the complete stability for all  $\kappa$  modes. On the other hand, it was also pointed out in Ref. [41] that the tunnelling process can occur when the energy of the Dirac field  $\omega^2$ , which is always larger than the mass  $m$ , is smaller than the peak value of the effective potential ( $V_{\max}$ ), then the QNMs exist only when  $m^2 < \omega^2 < V_{\max}$ .

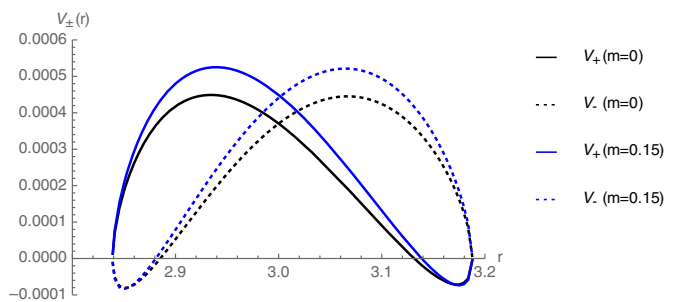


FIG. 1. The behavior of  $V_{\pm}(r)$  as a function of  $r$ , with  $M = 1$ , and  $\kappa = 1$ . Left panel for  $\Lambda = 0.04$ , and right panel for  $\Lambda = 0.11$ .

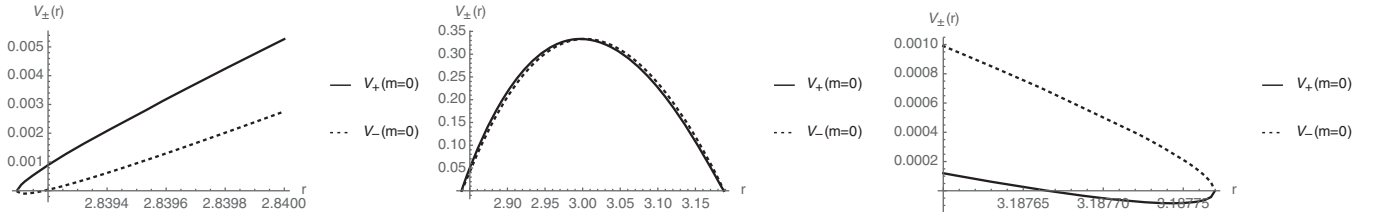


FIG. 2. The behavior of  $V_{\pm}(r)$  as a function of  $r$  for massless Dirac field, with  $M = 1$ ,  $\Lambda = 0.11$ , and  $\kappa = 30$ . Left panel for the region near  $r_H$ , center panel for the global behavior, and right panel for the region near  $r_{\Lambda}$ .

### III. QUASINORMAL MODES

Now, in order to obtain the QNFs, we shall solve numerically the generalized eigenvalue equation (8). We will only consider Eq. (8) because Eqs. (8) and (9) are isospectral, i.e., they possess the same QNM spectrum. Here, we use the pseudospectral Chebyshev method to find the QNM spectrum, see, for instance, Ref. [33]. Also, we will write only the QNFs with positive real part, because similar QNFs differing only in the sign of the real part are present in the spectrum. Now, we analyze the asymptotic behaviours of the radial function at the event and cosmological horizons along with the boundary conditions in both limits to accommodate the boundary conditions in the pseudospectral Chebyshev method. So, considering Eq. (8), in the vicinity of the horizon the function  $\psi_1(r)$  behaves as

$$\psi_1(r) = C_1(r - r_H)^{-i\omega/f'(r_H)} + C_2(r - r_H)^{1/2+i\omega/f'(r_H)}, \quad (16)$$

where, the first term represents an ingoing wave and the second represents an outgoing wave near the black hole horizon. So, imposing the requirement of only ingoing waves at the horizon, we fix  $C_2 = 0$ . On the other hand, at the cosmological horizon the function  $\psi_1(r)$  behaves as

$$R(y) = D_1(r - r_C)^{-i\omega/f'(r_C)} + D_2(r - r_C)^{1/2+i\omega/f'(r_C)}, \quad (17)$$

where, the first term represents an outgoing wave and the second represents an ingoing wave near the cosmological horizon. So, imposing the requirement of only ingoing waves on the cosmological horizon requires  $D_1 = 0$ . Therefore, taking into account the behavior of the scalar field at the event and cosmological horizons we define the following ansatz:

$$\psi_1(r) = (r - r_H)^{-i\omega/f'(r_H)}(r - r_C)^{1/2+i\omega/f'(r_C)}F(r). \quad (18)$$

Then, by inserting the above expression for  $\psi_1(r)$  in Eq. (8), it is possible to obtain an equation for the function  $F(r)$ . Also, it is convenient to perform a change of variable in order to limit the values of the radial coordinate to the range  $[0, 1]$ , thereby we define the change of variable  $y = (r - r_H)/(r_{\Lambda} - r_H)$ . So, the event horizon is located at

$y = 0$  and the cosmological horizon at  $y = 1$ . Thus, we have to solve an equation for a function of  $y$ , say  $F(y)$  which is regular at both, the event and cosmological horizons. To use the pseudospectral method,  $F(y)$  must be expanded in a complete basis of functions  $\varphi_i(y)$ :  $F(y) = \sum_{i=0}^{\infty} c_i \varphi_i(y)$ , where  $c_i$  are the coefficients of the expansion, and we choose the Chebyshev polynomials for the complete basis of functions, which are defined by  $T_j(x) = \cos(j \cos^{-1} x)$ , where  $j$  corresponds to the grade of the polynomial. The sum must be truncated until a  $N$  value, therefore the function  $F(y)$  can be approximated by

$$F(y) \approx \sum_{i=0}^N c_i T_i(x). \quad (19)$$

Thus, the solution is assumed to be a finite linear combination of the Chebyshev polynomials, that are well defined in the interval  $[-1, 1]$ . Due to the variable  $y$  being defined in the interval  $[0, 1]$ ,  $x$  and  $y$  are related by  $x = 2y - 1$ .

Then, the interval  $[0, 1]$  is discretized at the Chebyshev collocation points  $y_j$  by using the so-called Gauss-Lobatto grid where

$$y_j = \frac{1}{2} \left[ 1 - \cos\left(\frac{j\pi}{N}\right) \right], \quad j = 0, 1, \dots, N. \quad (20)$$

After that, the differential equation is evaluated at each collocation point. So, a system of  $N + 1$  algebraic equations is obtained, which corresponds to a generalized eigenvalue problem and it can be solved numerically to obtain the QNMs spectrum, by employing the built-in Eigensystem[ ] procedure in Wolframs *Mathematica* [46]. In this work, we use a value of  $N$  into the interval  $[80-120]$  with an average running time in the range  $[75s-245s]$  which depends on the convergence of  $\omega$  to the desired accuracy. We use an accuracy of eight decimal places with the exception of Table II, where we use an accuracy of five decimal places. In order to guarantee the accuracy of the results the code was executed for several increasing values of  $N$  until no difference was observed in the value of the QNF. Also, the complete parameter space associated to the models is  $mM \geq 0$ ,  $0 < \Lambda M^2 \leq 1/9$ , and  $\kappa = \pm(\ell + 1)$ , with  $\ell = 0, 1, 2, \dots$ . Here, the regions of the parameter space explored is  $0 \leq mM \leq 0.20$  due to the anomalous decay rate behavior observed for small values of  $mM$ ,

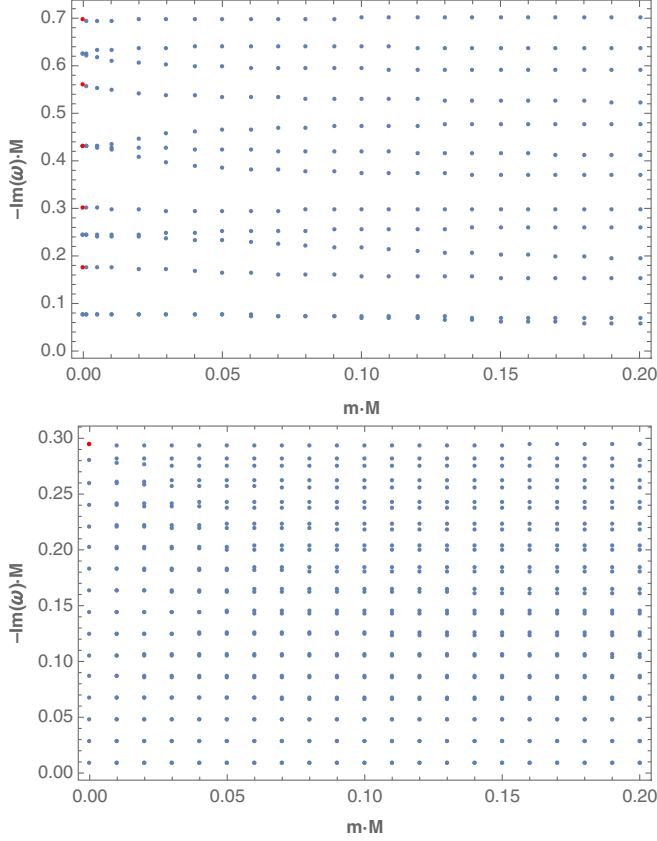
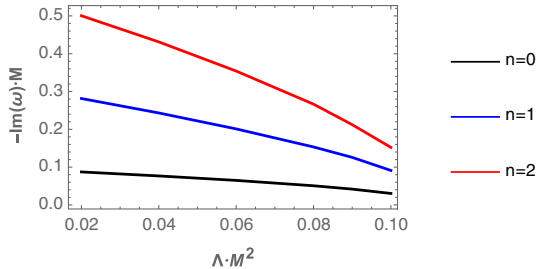


FIG. 3. The behavior of  $-\text{Im}(\omega)M$  as a function of  $mM$ , for  $\psi_1(r)$  with  $\kappa = 1$ . Top panel for  $\Lambda M^2 = 0.04$ , and bottom panel for  $\Lambda M^2 = 0.11$ . The red points correspond to purely imaginary QNFs while the blue points correspond to complex QNFs.

$0 < \Lambda M^2 \leq 0.11$ , and a discrete set of values of  $\kappa$  in the interval  $[1, 200]$ .

Now, in order to identify the different families of modes that are present in the fermionic spectrum, we plot in Fig. 3 the behavior of  $-\text{Im}(\omega)M$  versus the product of the fermionic field mass and black hole mass  $mM$ . The red points correspond to purely imaginary QNFs while that blue points correspond to complex QNFs. We can note the existence of two family of modes. One of them, corresponds to the de Sitter modes ( $\omega_{\text{dS}}$ ), in that they continuously approach those of empty de Sitter space in the limit



that the black hole mass vanishes. In this case, the QNFs for massless fermionic field are purely imaginary and they acquire a real part when the fermionic field is massive. The other family corresponds to the photon sphere (PS) modes ( $\omega_{\text{PS}}$ ), that are complex frequencies, and continuously approach those of Schwarzschild black hole when  $\Lambda \rightarrow 0$ . In the following we will study both families separately. Also, note that in Fig. 3 the fine structure related to the coupling between the chirality and the mass of the field appears spontaneously in the spectrum.

## A. Photon sphere modes

### 1. Massless fermionic fields

Now, we plot in Fig. 4 the behavior of  $-\text{Im}(\omega_{\text{PS}})M$  (left panel) and  $\text{Re}(\omega_{\text{PS}})M$  (right panel) as a function of  $\Lambda M^2$ , for massless fermionic fields and for the overtone numbers  $n_{\text{PS}} = 0, 1$ , and 2. We can observe that when the cosmological constant increases the decay rate and the frequency of the oscillation decreases. However, when the overtone number increases the decay rate increases and the frequency of the oscillations decreases.

On the other hand, it is known that the photon sphere modes are given by

$$\omega_{\text{PS}} = \frac{\sqrt{1 - 9M^2\Lambda}}{3\sqrt{3}M} \left( \ell - \left( n_{\text{PS}} + \frac{1}{2} \right) i \right), \quad (21)$$

which was obtained using the 1st-order WKB method [19]. Thus, in order to check the correctness and accuracy of the numerical technique with respect to previous results Eq. (21), we show in Table I the values obtained via the pseudospectral Chebyshev method and using Eq. (21) for high values of  $\kappa$ . Also, we show the relative error, which is defined by

$$\epsilon_{\text{Re}(\omega)} = \frac{|Re(\omega_1) - Re(\omega_0)|}{Re(\omega_0)} \cdot 100\%, \quad (22)$$

$$\epsilon_{\text{Im}(\omega)} = \frac{|Im(\omega_1) - Im(\omega_0)|}{Im(\omega_0)} \cdot 100\%, \quad (23)$$

where  $\omega_1$  corresponds to the result from Eq. (21) [19], and  $\omega_0$  denotes our result with the pseudospectral Chebyshev

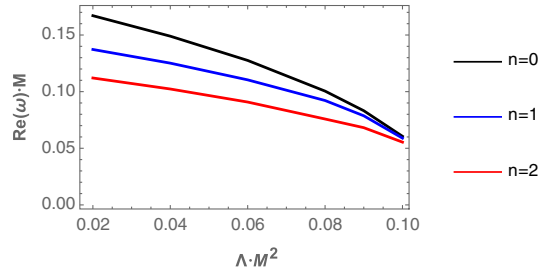


FIG. 4. The behavior of  $-\text{Im}(\omega_{\text{PS}})M$  (left) and  $\text{Re}(\omega_{\text{PS}})M$  (right) as a function of  $\Lambda M^2$  for massless fermionic fields with  $\kappa = 1$ , and different values of the overtone number  $n_{\text{PS}} = 0, 1$ , and 2.

TABLE I. Quasinormal frequencies  $\omega_{\text{PS}}M$  for massless fermionic fields with  $\kappa = 50, 100, 125, 150, 175$ , and  $200$  in the background of Schwarzschild–dS black holes, with  $\Lambda M^2 = 0.04$ .

$n_{\text{PS}} = 0$				
$\kappa$	Pseudospectral method	WKB	$\epsilon_{\text{Re}(\omega)}$	$\epsilon_{\text{Im}(\omega)}$
50	$7.69790323 - 0.07697990i$	$7.69800359 - 0.07698004i$	0.00130373	0.00018187
100	$15.39595700 - 0.07698000i$	$15.39600718 - 0.07698004i$	0.00032593	0.00005196
125	$19.24496883 - 0.07698001i$	$19.24500897 - 0.07698004i$	0.00020857	0.00003897
150	$23.09397731 - 0.07698002i$	$23.09401077 - 0.07698004i$	0.00014489	0.00002598
175	$26.94298389 - 0.07698002i$	$26.94301256 - 0.07698004i$	0.00010641	0.00002598
200	$30.79198927 - 0.07698003i$	$30.79201436 - 0.07698004i$	0.00008148	0.00001299
$n_{\text{PS}} = 1$				
$\kappa$	Pseudospectral method	WKB	$\epsilon_{\text{Re}(\omega)}$	$\epsilon_{\text{Im}(\omega)}$
50	$7.69735582 - 0.23094427i$	$7.69800359 - 0.23094011i$	0.00841549	0.00180130
100	$15.39568329 - 0.23094115i$	$15.39600718 - 0.23094011i$	0.00210377	0.00045033
125	$19.24474986 - 0.23094077i$	$19.24500897 - 0.23094011i$	0.00134639	0.00028579
150	$23.09379484 - 0.23094057i$	$23.09401077 - 0.23094011i$	0.00093501	0.00019919
175	$26.94282748 - 0.23094045i$	$26.94301256 - 0.23094011i$	0.00068694	0.00014722
200	$30.79185241 - 0.23094037i$	$30.79201436 - 0.23094011i$	0.00052595	0.00011258
$n_{\text{PS}} = 2$				
$\kappa$	Pseudospectral method	WKB	$\epsilon_{\text{Re}(\omega)}$	$\epsilon_{\text{Im}(\omega)}$
50	$7.69626106 - 0.38492238i$	$7.69800359 - 0.38490011i$	0.02264125	0.00578558
100	$15.39513589 - 0.38490573i$	$15.39600718 - 0.38490011i$	0.00565952	0.00146010
125	$19.24431194 - 0.38490373i$	$19.24500897 - 0.38490011i$	0.00362201	0.00094049
150	$23.09342991 - 0.38490265i$	$23.09401077 - 0.38490011i$	0.00251526	0.00065991
175	$26.94251468 - 0.38490199i$	$26.94301256 - 0.38490011i$	0.00184793	0.00048844
200	$30.79157871 - 0.38490157i$	$30.79201436 - 0.38490011i$	0.00141484	0.00037932

method. We can observe that the error does not exceed 0.006% in the imaginary part, and 0.023% in the real part. Also, as it was observed, the frequencies all have a negative imaginary part, which means that the propagation of massless fermionic field is stable in this background.

## 2. Massive fermionic fields

In this section, we will consider the propagation of massive fermionic fields, as we will see, the two chiralities of massive fermions lead to an additional fine structure in the spectrum, as the one reported for Schwarzschild and Kerr backgrounds by using the convergent Frobenius method [43], and contrary to massless case, where the fine structure is not present, thereby the coupling between the chirality and the mass of the field leads to a fine structure in the spectrum of the QNMs. Also, we will show that the anomalous behavior of the decay rate of the fermionic QNMs is present in this family, depending on the values of  $\Lambda M^2$ , as well as a critical fermionic field mass.

*Fine structure.*—As we mentioned, it is possible to observe a spontaneous split of the QNFs by using the pseudospectral Chebyshev method when  $m \neq 0$ , which leads to a fine

structure in the fermionic spectrum and it is associated to the two chiralities of the field. In spite of the specific representation used in the Dirac equation does not allow us to appreciate the positive and negative chirality easily. We consider the modes with positive chirality as those with higher oscillation frequency, which was shown for  $\Lambda = 0$  in Ref. [43], and it allows us to distinguish between both chiralities. In Fig. 5 we plot the behavior of  $-\text{Im}(\omega_{\text{PS}})M$  (left panel) and  $\text{Re}(\omega_{\text{PS}})M$  (right panel) as a function of  $\Lambda M^2$  for  $n_{\text{PS}} = 0$  and  $mM = 0, 0.05$ , the numerical values are given in Table II. So, by considering as fine structure the splitting generated in the QNFs, which occurs for  $mM \neq 0$ , in Fig. 5 we show the effect of  $\Lambda M^2$  on the fine structure for  $mM = 0.05$ , where we can observe that the splitting in the real part (right panel), decreases when  $\Lambda M^2$  increases, and it go to zero when the black hole becomes extremal. For the imaginary part (left panel), we observe that there is a value of  $\Lambda M^2$  where the curves intersect, i.e., the fine structure vanishes. Before this point, the fine structure decreases when  $\Lambda M$  increases and after it the behavior is inverted. Then, the fine structure decreases and vanishes again when the black hole becomes extremal. For  $mM = 0$  we do not observe a fine structure (black curve).

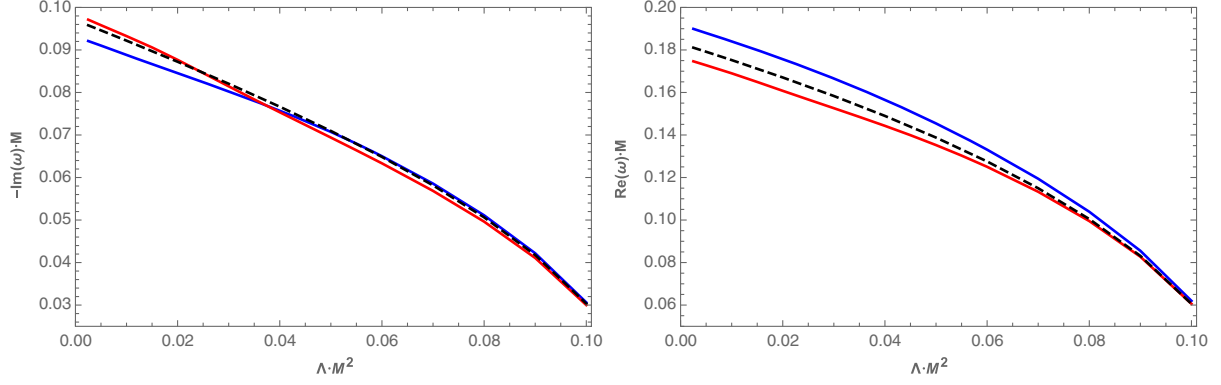


FIG. 5. The behavior of  $-\text{Im}(\omega_{\text{PS}})M$  (left panel), and  $\text{Re}(\omega_{\text{PS}})M$  (right panel) obtained through the pseudospectral Chebyshev method, as a function of  $\Lambda M^2$ , for  $\kappa = 1$ . Black dashed line for  $mM = 0$ , blue line for  $mM = 0.05$  and positive chirality, and red line for  $mM = 0.05$  and negative chirality.

Now, in order to study the effect of  $mM$  on the fine structure, we plot in Fig. 6 the behavior of the QNFs versus  $mM$  for  $\Lambda M^2 = 0.01$  and  $\kappa = 1$  (top panels), and  $\kappa = 10$  (bottom panels), for small values of  $mM$ . So, we can observe that the fine structure, in the imaginary part, decreases when the parameter  $\kappa$  increases, or in other words, the fine structure is finer for higher values of  $\kappa$ . However, it increases with  $mM$ , and the same behavior occurs for the real part of the fine structure.

*Anomalous decay rate.*—As we mentioned, the anomalous decay rate behavior occurs when the longest-lived modes are the ones with higher angular number, while that the existence of a critical scalar field mass indicates that beyond this value the anomalous decay rate behavior is inverted [26,29]. In order to visualize this behavior, in Fig. 7 we plot  $-\text{Im}(\omega_{\text{PS}})M$  as a function of  $mM$ , for different values of the cosmological constant  $\Lambda M^2 = 0.01, 0.04, \text{ and } 0.11$  and for different values of the parameter  $\kappa = 5, 30, \text{ and } 100$  by using the pseudospectral Chebyshev

method. We can observe for small values of  $\Lambda M^2 = 0.01$  (top panels) that the anomalous decay rate in the QNFs is present, as well as, the existence of a critical mass, where the behavior is inverted; however, for  $\Lambda M^2 = 0.04$  (center panels) and for near extremal black hole  $\Lambda M^2 = 0.11$  (bottom panels), the pseudospectral Chebyshev method predicts that there is not such anomalous behavior, and also there is not a critical mass for the fermionic field, except for the case  $\Lambda M^2 = 0.11$  and positive chirality (right-bottom panel) where we can observe an anomalous behavior and a small critical mass. So, the existence of the anomalous decay rate depends on the value of  $\Lambda M^2$ , and the existence of the critical mass depends on  $\Lambda M^2$  and the chirality, for the cases considered here.

Now, we shall employ the Wentzel-Kramers-Brillouin (WKB) approach in order to get some analytical insight on the behavior of the QNFs in the eikonal limit  $\kappa \rightarrow \infty$ . The WKB approximation was initiated by Mashhoon [47] and by Schutz and Iyer [48]. Then, Iyer and Will computed the third order correction [49], and it was extended to the sixth

TABLE II. Quasinormal frequencies  $\omega_{\text{PS}}M$  obtained through the pseudospectral Chebyshev method for fermionic fields with  $\kappa = 1$ , in the background of Schwarzschild–dS black holes.

$n_{\text{PS}} = 0$	$mM = 0.05$		
$\Lambda M^2$	$mM = 0$	Positive chirality	Negative chirality
0.0025	$0.18107 - 0.09580i$	$0.18992 - 0.09210i$	$0.17466 - 0.09712i$
0.005	$0.17916 - 0.09461i$	$0.18796 - 0.09103i$	$0.17280 - 0.09583i$
0.01	$0.17524 - 0.09219i$	$0.18395 - 0.08885i$	$0.16901 - 0.09326i$
0.02	$0.16706 - 0.08723i$	$0.17568 - 0.08452i$	$0.16078 - 0.08767i$
0.03	$0.15835 - 0.08206i$	$0.16661 - 0.08027i$	$0.15261 - 0.08145i$
0.04	$0.14898 - 0.07666i$	$0.15652 - 0.07573i$	$0.14431 - 0.07535i$
0.05	$0.13879 - 0.07096i$	$0.14538 - 0.07069i$	$0.13526 - 0.06940i$
0.06	$0.12756 - 0.06485i$	$0.13310 - 0.06501i$	$0.12504 - 0.06334i$
0.07	$0.11496 - 0.05816i$	$0.11942 - 0.05857i$	$0.11330 - 0.05686i$
0.08	$0.10048 - 0.05064i$	$0.10389 - 0.05111i$	$0.09952 - 0.04962i$
0.09	$0.08315 - 0.04177i$	$0.08554 - 0.04218i$	$0.08274 - 0.04108i$
0.1	$0.06058 - 0.03036i$	$0.06198 - 0.03062i$	$0.06059 - 0.03000i$

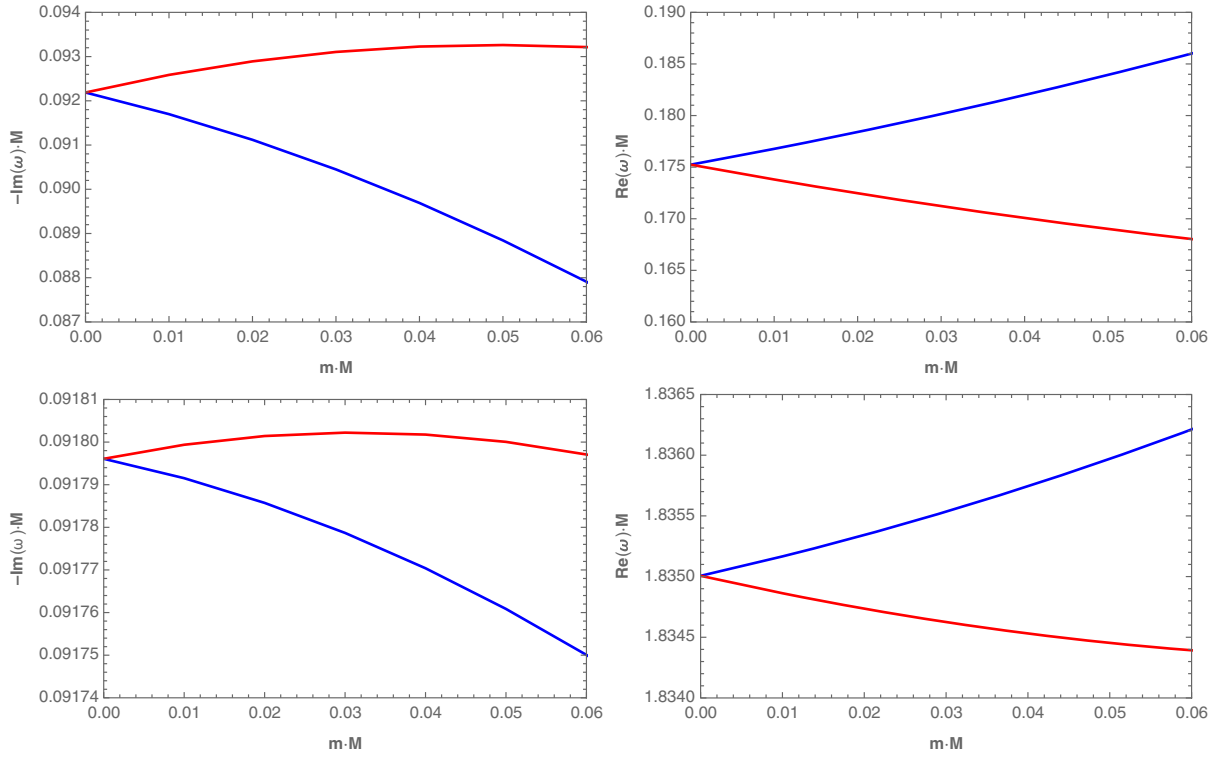


FIG. 6. The behavior of  $-\text{Im}(\omega_{\text{PS}})M$  (left panels), and  $\text{Re}(\omega_{\text{PS}})M$  (right panels) obtained through the pseudospectral Chebyshev method, as a function of  $mM$ , for  $\kappa = 1$  (top panels), and  $\kappa = 10$  (bottom panels), with  $\Lambda M^2 = 0.01$ . Blue line for positive chirality and red line for negative chirality.

order [50], and up to the 13th order [51], see also Ref. [52]. This method has been used to determine the QNFs for asymptotically flat and asymptotically de Sitter black holes. This is due to that the WKB method can be used for effective potentials which have the form of potential barriers that approach to a constant value at the horizon and spatial infinity [4]. The QNMs are determined by the behavior of the effective potential near its maximum value  $r_{\text{max}}^*$ . The Taylor series expansion of the potential around its maximum is given by

$$V(r^*) = V(r_{\text{max}}^*) + \sum_{i=2}^{i=\infty} \frac{V^{(i)}}{i!} (r^* - r_{\text{max}}^*)^i, \quad (24)$$

where

$$V^{(i)} = \frac{d^i}{dr^{*i}} V(r^*)|_{r^*=r_{\text{max}}^*}, \quad (25)$$

corresponds to the  $i$ th derivative of the potential with respect to  $r^*$  evaluated at the maximum of the potential  $r_{\text{max}}^*$ . Using the WKB approximation up to 6th order the QNFs are given by the following expression [53]:

$$\omega_{\text{PS}}^2 = V(r_{\text{max}}^*) - 2iU, \quad (26)$$

where

$$\begin{aligned} U = & N\sqrt{-V^{(2)}/2} + \frac{i}{64} \left( -\frac{1}{9} \frac{V^{(3)2}}{V^{(2)2}} (7 + 60N^2) + \frac{V^{(4)}}{V^{(2)}} (1 + 4N^2) \right) \\ & + \frac{N}{2^{3/2} 288} \left( \frac{5}{24} \frac{V^{(3)4}}{(-V^{(2)})^{9/2}} (77 + 188N^2) + \frac{3}{4} \frac{V^{(3)2} V^{(4)}}{(-V^{(2)})^{7/2}} (51 + 100N^2) \right. \\ & \left. + \frac{1}{8} \frac{V^{(4)2}}{(-V^{(2)})^{5/2}} (67 + 68N^2) + \frac{V^{(3)} V^{(5)}}{(-V^{(2)})^{5/2}} (19 + 28N^2) + \frac{V^{(6)}}{(-V^{(2)})^{3/2}} (5 + 4N^2) \right), \end{aligned}$$

and  $N = n_{\text{PS}} + 1/2$ , with  $n_{\text{PS}} = 0, 1, 2, \dots$ , is the overtone number. We will consider only the effective potential  $V_+(r)$  with the plus sign in Eq. (14) due to  $V_-$  yields the same QNFs. Note that in this case the potential also depends on the frequencies, so the evaluation of the QNFs is more difficult; however, our interest is to evaluate the QNFs for large values



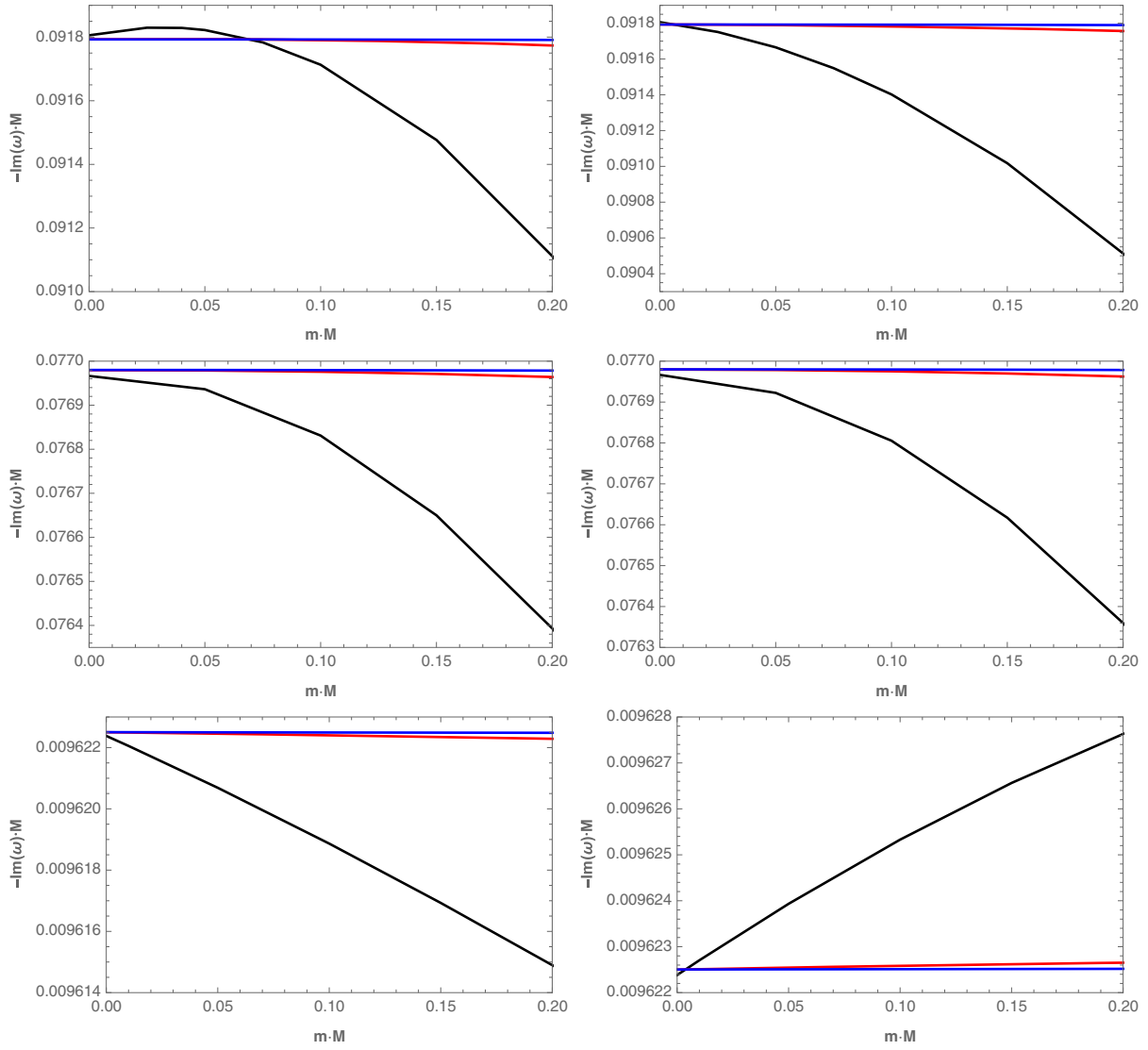


FIG. 7. The behavior of  $-\text{Im}(\omega_{\text{PS}})M$  obtained through the pseudospectral Chebyshev method as a function of  $mM$  with  $\kappa = 5$  (black line),  $\kappa = 30$  (red line), and  $\kappa = 100$  (blue line).  $\Lambda M^2 = 0.01$  (top panel),  $\Lambda M^2 = 0.04$  (central panel), and  $\Lambda M^2 = 0.11$  (bottom panel). Left (right) panels for the negative (positive) chirality.

of  $\kappa$ , so we expand the frequencies as a power series in  $\kappa$ . In the previous section, we showed in Eq. (21) that in the eikonal limit the leading order term is linear in  $\ell$ , so we consider the following expansion of the frequency in powers of  $\kappa$

$$\omega_{\text{PS}} = \omega_1 \kappa + \omega_0 + \omega_{-1} \kappa^{-1} + \omega_{-2} \kappa^{-2}. \quad (27)$$

We find that for large values of  $\kappa$ , the maximum of the potential is approximately at

$$\begin{aligned} r_{\text{max}} \approx & 3M - \frac{\sqrt{3}}{2} M \sqrt{1 - 9\Lambda M^2} \kappa^{-1} - \frac{(1 - 9\Lambda M^2)(1 - 9M^2(\Lambda + 3m\omega_1))mM}{3\omega_1} \kappa^{-2} \\ & + \frac{M\sqrt{1 - 9\Lambda M^2}}{48\sqrt{3}\omega_1^2} (3(11 - 18\Lambda M^2)\omega_1^2 - 108(mM)^2\omega_1^2(1 - 36\Lambda M^2)) \\ & + 4m(1 - 9\Lambda M^2)(4\sqrt{3}\omega_0\sqrt{1 - 9\Lambda M^2} + \omega_1(1 - 36\Lambda M^2))\kappa^{-3}, \end{aligned} \quad (28)$$

and

$$V(r_{\max}^*) \approx \frac{(1-9\Lambda M^2)}{27M^2} \kappa^2 - \frac{(1-9\Lambda M^2)(4m(1-9M^2(\Lambda+3m\omega_1)) - 3m\omega_1)}{324M^2\omega_1} + \frac{(1-9\Lambda M^2)(6m(1-9\Lambda M^2)\omega_0 + \sqrt{3}\sqrt{1-9\Lambda M^2}\omega_1^2)}{486M^2\omega_1^2} \kappa^{-1}, \quad (29)$$

and the second derivative of the effective potential evaluated at  $r_{\max}^*$  yields

$$V_{r_{\max}^*}^{(2)} \approx -\frac{2(1-9\Lambda M^2)^2}{729M^4} \kappa^2 + \frac{(1-9\Lambda M^2)^2(4m(1+9\Lambda M^2(4-45\Lambda M^2)) - 15\omega_1 + 54\omega_1 M^2(m^2(4-90\Lambda M^2) + \Lambda))}{13122\omega_1 M^4}. \quad (30)$$

The higher derivatives are given by

$$V_{r_{\max}^*}^{(3)} \approx \frac{4(1-9\Lambda M^2)^3}{6561M^5} \kappa^2 - \frac{(1-9\Lambda M^2)^{5/2}}{729\sqrt{3}M^5} \kappa, \quad (31)$$

$$V_{r_{\max}^*}^{(4)} \approx \frac{16(1-9\Lambda M^2)^3}{19683M^6} \kappa^2 + \frac{20(1-9\Lambda M^2)^{7/2}}{19683\sqrt{3}M^6} \kappa, \quad (32)$$

$$V_{r_{\max}^*}^{(5)} \approx -\frac{40(1-9\Lambda M^2)^4}{59049M^7} \kappa^2, \quad (33)$$

$$V_{r_{\max}^*}^{(6)} \approx -\frac{16(1-9\Lambda M^2)^4(4+15\Lambda M^2)}{177147M^8} \kappa^2, \quad (34)$$

where the leading and subleading terms are important for  $V_{r_{\max}^*}^{(3)}$  and  $V_{r_{\max}^*}^{(4)}$ , and only the leading terms of the expansion are important for  $V_{r_{\max}^*}^{(5)}$  and  $V_{r_{\max}^*}^{(6)}$  in the limit considered. Thus, using these results and  $n_{\text{PS}} = 0$  we obtain  $U$  evaluated at  $r_{\max}^*$

$$U = (1-9\Lambda M^2) \left( \frac{1}{54M^2} \kappa - i \frac{65-99\Lambda M^2}{5832M^2} - \left( \frac{216m(1-9\Lambda M^2)(1+45\Lambda M^2) + 5832m^2 M^2(2-45\Lambda M^2)\omega_1}{209952M^2\omega_1} + \frac{(169+216\sqrt{3}i\sqrt{1-9\Lambda M^2} - 9\Lambda M^2(14+1395\Lambda M^2))\omega_1}{209952M^2\omega_1} \right) \kappa^{-1} \right), \quad (35)$$

and then replacing these expansions in Eq. (26) and solving order by order for  $\omega_i$  we obtain the following QNFs for  $n_{\text{PS}} = 0$

$$\omega_{\text{PS}} M = \sqrt{1-9\Lambda M^2} \left( \left( \frac{1}{3\sqrt{3}} \kappa - \frac{11\sqrt{3}(1-9\Lambda M^2) + 324mM\sqrt{1-9\Lambda M^2} - 972\sqrt{3}(mM)^2}{1944} \kappa^{-1} \right) - i \left( \frac{1}{6\sqrt{3}} + \frac{\sqrt{3}(29-1395\Lambda M^2)(1-9\Lambda M^2) + 9720mM(1-9\Lambda M^2)\sqrt{1-9\Lambda M^2} - 29160\sqrt{3}(mM)^2(1-9\Lambda M^2)}{69984} \kappa^{-2} \right) \right). \quad (36)$$

Notice that for  $m = 0$  we recover the result (21) for  $\ell \gg 1$ . Now, in Fig. 8, we show the behavior of  $-\text{Im}(\omega_{\text{PS}})M$  given by Eq. (36) as a function of  $mM$ , for different values of the cosmological constant  $\Lambda M^2 = 0.01, 0.04$ , and  $0.11$  and for different values of the parameter  $\kappa = 5, 10, 20$ , and  $30$ . We can observe that for small values of  $\Lambda M^2 = 0.01$  the anomalous decay rate of the QNFs of massive fermionic fields in Schwarzschild–de Sitter black holes backgrounds is present, in which the longest-lived modes are the ones with higher angular number, for a fermionic field mass smaller than a critical value, while that beyond this value the behavior is inverted (top left panel). Then, when we increase the value of  $\Lambda M^2$  to  $0.04$ , it is possible to observe (top right panel), the existence of two zones where the longest-lived modes are the ones with smaller angular number, for small and large mass of the fermionic field, and also a central zone where the anomalous behavior in the decay rate of the QNFs is present. Also, it is possible to observe the existence of two values of critical mass, where the behavior of the decay rate of the QNF is inverted. Finally, by increasing the value of  $\Lambda M^2$  to  $0.11$ , we can observe (bottom panel) that the anomalous behavior is not present and the longest-lived modes are the ones with smaller angular number for all the range of fermionic field mass.

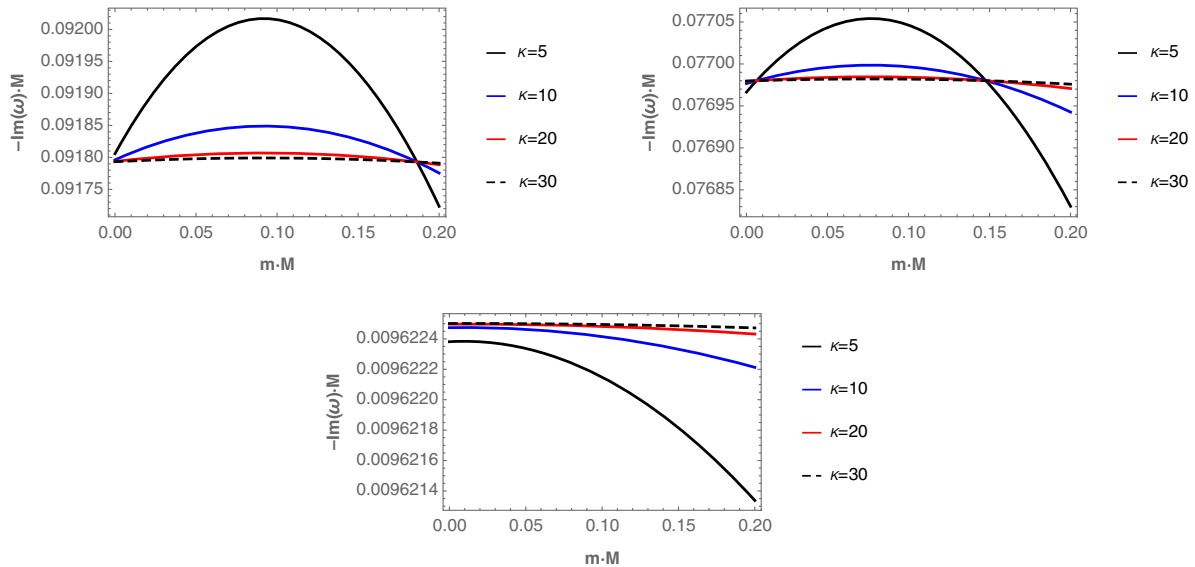


FIG. 8. The behavior of  $-\text{Im}(\omega_{\text{PS}})M$  obtained through the WKB method as a function of  $mM$  with  $\kappa = 5, 10, 20, 30$ , and  $\Lambda M^2 = 0.01$  (top left panel),  $\Lambda M^2 = 0.04$  (top right panel), and  $\Lambda M^2 = 0.11$  (bottom panel).

The critical mass  $m_c$  corresponds to the value of the mass for which the term proportional to  $\kappa^{-2}$  of  $\text{Im}(\omega_{\text{PS}})M$  vanishes, thereby

$$m_c M \approx \frac{90(1 - 9\Lambda M^2) \pm \sqrt{30}\sqrt{(299 - 3825\Lambda M^2)(1 - 9\Lambda M^2)}}{540\sqrt{3}\sqrt{1 - 9\Lambda M^2}}. \quad (37)$$

The critical mass depends on the values of  $\Lambda M^2$ . In some cases there is no critical mass, one critical mass or two critical masses, see Fig. 8. In the case of one critical mass, for  $m > m_c$ ,  $\omega_{\text{PS}}$  increases with  $\kappa$ ; whereas, for  $m < m_c$ ,  $-\text{Im}(\omega_{\text{PS}})$  decreases when  $\kappa$  increases. Also, for  $\Lambda \rightarrow 0$ , we obtain the critical mass  $m_c M \approx 0.1975$ . On the other hand, when  $\Lambda M^2$  increases the critical mass decreases and for values of  $\Lambda M^2$  bigger than the critical value  $\Lambda_c M^2 = 299/3825 \approx 0.0782$  there is no critical mass.

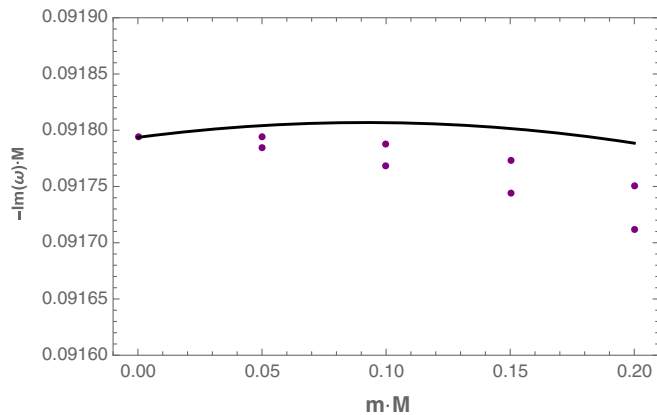


FIG. 9. The behavior of  $-\text{Im}(\omega_{\text{PS}})M$  as a function of  $mM$ , for  $\kappa = 20$  and  $\Lambda M^2 = 0.01$ . Black line is obtained by using the WKB method Eq. (36), and the purple points are obtained by using the pseudospectral Chebyshev method.

It is worth mentioning that by using the WKB method it is not possible to observe the fine structure in the spectrum, contrary to the pseudospectral Chebyshev method, where the fine structure appears spontaneously. Moreover, In Fig. 9, we show the behavior of  $-\text{Im}(\omega)M$  by using Eq. (36) (black line), and by using the pseudospectral Chebyshev method (purple points), as a function of  $mM$ , for  $\Lambda M^2 = 0.01$ , and  $\kappa = 20$ , we can observe the difference in the  $-\text{Im}(\omega)M$  for both methods. We attribute the discrepancy in the value of the critical mass in both methods, WKB and numerical, to the assertion that the WKB approach is not very accurate for the case of massive

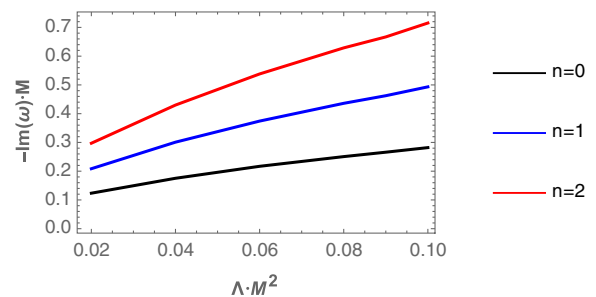


FIG. 10. The behavior of  $-\text{Im}(\omega_{\text{dS}})M$  obtained through the pseudospectral Chebyshev method as a function of  $\Lambda M^2$  for massless fermionic fields with  $\kappa = 1$ , and different values of the overtone number  $n_{\text{dS}} = 0, 1, \text{ and } 2$ .

TABLE III. Quasinormal frequencies  $\omega_{\text{dS}}M$  for massless fermionic fields obtained through the pseudospectral Chevsyshev method for different values of  $\kappa$  in the background of Schwarzschild–dS black holes with  $\Lambda M^2 = 0.04$ .

$\kappa$	$n_{\text{dS}} = 0$	$n_{\text{dS}} = 1$	$n_{\text{dS}} = 2$
1	$-0.175313983i$	$-0.300886899i$	$-0.429950083i$
2	$-0.289834484i$	$-0.410535743i$	$-0.534933226i$
3	$-0.404895443i$	$-0.523977837i$	$-0.645964460i$
10	$-1.212651098i$	$-1.329255647i$	$-1.44693078i$

fermionic field, this is because the WKB method strictly cannot be applied to the massive case, due to the effective potential allows another local minimum, so that the problem has now three turning points, as was proved in Ref. [43]. So, the WKB approach fails to give the accurate value of the critical mass.

### B. de Sitter modes

The de Sitter family consists of the modes that continuously approach to the QNMs of pure de Sitter spacetime when  $M \rightarrow 0$ . The frequencies of QNMs in pure de Sitter spacetime are given by [45]

$$\omega = -m - i\sqrt{\frac{\Lambda}{3}}\left(2n_{\text{dS}} + \kappa_+ + \frac{3}{2}\right),$$

$$\text{or } \omega = m - i\sqrt{\frac{\Lambda}{3}}\left(2n_{\text{dS}} + \kappa_+ + \frac{1}{2}\right), \quad (38)$$

and

$$\omega = -m - i\sqrt{\frac{\Lambda}{3}}\left(2n_{\text{dS}} - \kappa_- + \frac{1}{2}\right),$$

$$\text{or } \omega = m - i\sqrt{\frac{\Lambda}{3}}\left(2n_{\text{dS}} - \kappa_- - \frac{1}{2}\right), \quad (39)$$

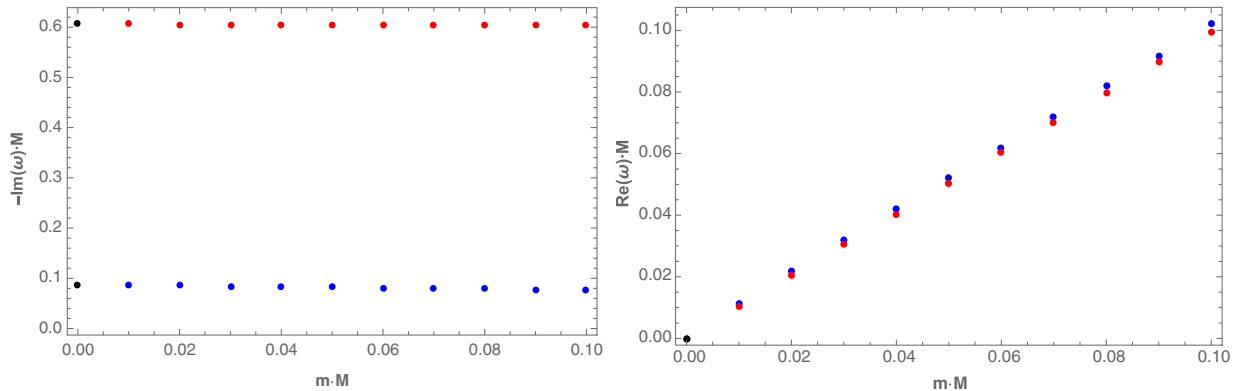


FIG. 11. The behavior of  $-\text{Im}(\omega_{\text{dS}})M$  (left panel), and  $\text{Re}(\omega_{\text{dS}})M$  (right panel) obtained through the pseudospectral Chevsyshev method as a function of  $mM$ , for  $\kappa = 1$  (blue points), and  $\kappa = 10$  (red points), with  $\Lambda M^2 = 0.01$ .

where  $\kappa_+$  and  $\kappa_-$  are positive and negative integers, respectively, and  $n_{\text{dS}} = 0, 1, 2, \dots$

Now, in order to visualize the behavior of the dS modes obtained through the pseudospectral Chevsyshev method we plot  $-\text{Im}(\omega_{\text{dS}})M$  as a function of  $\Lambda M^2$  in Fig. 10 for massless fermionic fields with  $\kappa = 1$ , and different values of the overtone number  $n_{\text{dS}} = 0, 1$ , and 2. First, we can observe that for small values of  $\Lambda M^2$ , the dS modes tend to the pure de Sitter modes with  $\kappa = \kappa_+ = -\kappa_- = 1$ . Also, the decay rate increases when  $\Lambda M^2$  or the overtone number increases. However, the dS modes are present in a range of value of  $\kappa$  and  $n_{\text{dS}}$ , see Table III.

Now, in order to observe the behavior of the dS modes we plot in Fig. 11 the QNFs as a function of  $mM$  for  $\kappa = 1$  (blue points), and  $\kappa = 10$  (red points), with  $\Lambda M^2 = 0.01$ , and  $n_{\text{dS}} = 0$ . The black points indicate a purely imaginary QNFs, that occurs for  $mM = 0$ , then this family acquires a real part. We can observe that the decay rate increases when the angular number increases, and exhibits a smooth behavior when  $mM$  increases (left panel). On the other hand, the frequency of the oscillations increases when  $mM$  increases and when the angular number decreases (right panel).

### IV. FINAL REMARKS

We considered the propagation of fermionic fields in the background of Schwarzschild–de Sitter black holes. Then, we showed the existence of two families of QNMs, one of them corresponds to the photon sphere modes and the other one to the dS modes. Mainly, we showed that it is possible to observe a fine structure in the spectrum, and also an anomalous behavior for the photon sphere modes, and it is not possible to observe the same for the dS modes. Also, both families present frequencies with a negative imaginary part, which means that the propagation of fermionic field is stable in this background for the values of the parameters that we considered; however, due to the existence of negative gaps in the potentials the stability is not evident and it could be studied via the time-domain integration of

the scalar wave equation as was performed for massless Dirac field on Schwarzschild–de Sitter black holes [39].

Our analysis was performed by using the pseudospectral Chebyshev method, and the WKB approach. However, while the results for massless fermionic field are similar with a small percentage of error, for massive fermionic field, the results are different and show different behaviors. The difference is due to the assertion that the WKB approach is not very accurate for the case of massive fermionic field, this is because the WKB method strictly cannot be applied to the massive case, due to the effective potential allows another local minimum, so that the problem has now three turning points, as was proved in Ref. [43].

Our conclusions are based on pseudospectral Chebyshev method, where the fine structure related to the coupling between the chirality and the mass of the field appears spontaneously in the spectrum, contrary to the WKB where we cannot observe the fine structure. We showed that the fine structure is proper of the photon sphere modes, and the separation in the  $-\text{Im}(\omega_{\text{PS}})M$  and  $\text{Re}(\omega_{\text{PS}})M$  between the modes with positive and negative chirality decreases when the parameter  $\kappa$  increases, it increases for higher overtone numbers, and it is more finer when  $\Lambda M^2$  increases.

Also, the decay rate of QNMs of fermionic perturbations show an anomalous behavior and the presence of a critical

fermionic field mass for small values of  $\Lambda M^2$ , for intermediate values we showed that there is not anomalous behavior either critical fermionic field mass. However, for higher values, i.e., when the black hole becomes near extremal, we found an anomalous decay rate for the modes associated with a positive chirality and a small fermionic field critical mass. While that for the modes associated with a negative chirality there is not an anomalous behavior either fermionic field critical mass. Also, we showed that there is a value of  $\Lambda M^2$  where the imaginary parts of the modes with positive and negative chirality coincide, before this value the modes with positive chirality are longer lived than the modes with negative chirality, and for higher values of  $\Lambda M^2$  the behavior is inverted, the modes with negative chirality become longer lived.

## ACKNOWLEDGMENTS

We thank the referee for his/her careful review of the manuscript and his/her valuable comments and suggestions which helped us to improve the manuscript. Y. V. acknowledges support by the Dirección de Investigación y Desarrollo de la Universidad de La Serena, Grant No. PR18142.

- 
- [1] T. Regge and J. A. Wheeler, Stability of a Schwarzschild singularity, *Phys. Rev.* **108**, 1063 (1957).
  - [2] F. J. Zerilli, Gravitational field of a particle falling in a Schwarzschild geometry analyzed in tensor harmonics, *Phys. Rev. D* **2**, 2141 (1970).
  - [3] H. P. Nollert, Topical review: Quasinormal modes: The characteristic ‘sound’ of black holes and neutron stars, *Classical Quantum Gravity* **16**, R159 (1999).
  - [4] R. A. Konoplya and A. Zhidenko, Quasinormal modes of black holes: From astrophysics to string theory, *Rev. Mod. Phys.* **83**, 793 (2011).
  - [5] K. D. Kokkotas and B. G. Schmidt, Quasinormal modes of stars and black holes, *Living Rev. Relativity* **2**, 2 (1999).
  - [6] B. P. Abbott *et al.* (LIGO Scientific and Virgo Collaborations), Observation of Gravitational Waves from a Binary Black Hole Merger, *Phys. Rev. Lett.* **116**, 061102 (2016).
  - [7] B. P. Abbott *et al.* (LIGO Scientific and Virgo Collaborations), Tests of General Relativity with GW150914, *Phys. Rev. Lett.* **116**, 221101 (2016).
  - [8] A. Strominger, The dS/CFT correspondence, *J. High Energy Phys.* **10** (2001) 034.
  - [9] E. Abdalla, B. Wang, A. Lima-Santos, and W. G. Qiu, Support of dS/CFT correspondence from perturbations of three-dimensional space-time, *Phys. Lett. B* **538**, 435 (2002).
  - [10] E. Abdalla, K. H. C. Castello-Branco, and A. Lima-Santos, Support of dS/CFT correspondence from space-time perturbations, *Phys. Rev. D* **66**, 104018 (2002).
  - [11] F. Mellor and I. Moss, Stability of black holes in De Sitter space, *Phys. Rev. D* **41**, 403 (1990).
  - [12] S. Chandrasekhar, *The Mathematical Theory of Black Holes* (Oxford University Press, New York, 1983).
  - [13] H. Otsuki and T. Futamase, Gravitational perturbation of Schwarzschild-de Sitter spacetime and its quasi-normal modes, *Prog. Theor. Phys.* **85**, 771 (1991).
  - [14] P. R. Brady, C. M. Chambers, W. Krivan, and P. Laguna, Telling tails in the presence of a cosmological constant, *Phys. Rev. D* **55**, 7538 (1997).
  - [15] P. R. Brady, C. M. Chambers, W. G. Laarakkers, and E. Poisson, Radiative falloff in Schwarzschild–de Sitter spacetime, *Phys. Rev. D* **60**, 064003 (1999).
  - [16] V. Cardoso and J. P. Lemos, Quasinormal modes of the near extremal Schwarzschild–de Sitter black hole, *Phys. Rev. D* **67**, 084020 (2003).
  - [17] I. G. Moss and J. P. Norman, Gravitational quasinormal modes for anti-de Sitter black holes, *Classical Quantum Gravity* **19**, 2323 (2002).
  - [18] V. Suneeta, Quasinormal modes for the SdS black hole: An analytical approximation scheme, *Phys. Rev. D* **68**, 024020 (2003).

- [19] A. Zhidenko, Quasinormal modes of Schwarzschild de Sitter black holes, *Classical Quantum Gravity* **21**, 273 (2004).
- [20] R. A. Konoplya and A. Zhidenko, High overtones of Schwarzschild-de Sitter quasinormal spectrum, *J. High Energy Phys.* **06** (2004) 037.
- [21] C. Molina, D. Giugno, E. Abdalla, and A. Saa, Field propagation in de Sitter black holes, *Phys. Rev. D* **69**, 104013 (2004).
- [22] T. R. Choudhury and T. Padmanabhan, Quasinormal modes in Schwarzschild–deSitter space-time: A simple derivation of the level spacing of the frequencies, *Phys. Rev. D* **69**, 064033 (2004).
- [23] Y. Zhang, E. K. Li, and J. L. Geng, Quasinormal modes of massless scalar field perturbation of a Reissner-Nordström de Sitter black hole with a global monopole, *Gen. Relativ. Gravit.* **46**, 1728 (2014).
- [24] B. Toshmatov and Z. Stuchlik, Slowly decaying resonances of massive scalar fields around Schwarzschild-de Sitter black holes, *Eur. Phys. J. Plus* **132**, 324 (2017).
- [25] A. Jansen, Overdamped modes in Schwarzschild-de Sitter and a *Mathematica* package for the numerical computation of quasinormal modes, *Eur. Phys. J. Plus* **132**, 546 (2017).
- [26] A. Aragón, P. A. González, E. Papantonopoulos, and Y. Vásquez, Anomalous decay rate of quasinormal modes in Schwarzschild-dS and Schwarzschild-AdS black holes, *J. High Energy Phys.* **08** (2020) 120.
- [27] V. Cardoso, J. L. Costa, K. Destounis, P. Hintz, and A. Jansen, Quasinormal Modes and Strong Cosmic Censorship, *Phys. Rev. Lett.* **120**, 031103 (2018).
- [28] M. Zhang, J. Jiang, and Z. Zhong, Relaxation rate of RNdS black hole, *Phys. Lett. B* **806**, 135523 (2020).
- [29] M. Lagos, P. G. Ferreira, and O. J. Tattersall, Anomalous decay rate of quasinormal modes, *Phys. Rev. D* **101**, 084018 (2020).
- [30] A. Aragón, P. A. González, E. Papantonopoulos, and Y. Vásquez, Quasinormal modes and their anomalous behavior for black holes in  $f(R)$  gravity, [arXiv:2005.11179](https://arxiv.org/abs/2005.11179).
- [31] R. D. B. Fontana, P. A. González, E. Papantonopoulos, and Y. Vásquez, Anomalous decay rate of quasinormal modes in Reissner-Nordström black holes, [arXiv:2011.10620](https://arxiv.org/abs/2011.10620).
- [32] K. Destounis, R. D. B. Fontana, and F. C. Mena, Accelerating black holes: Quasinormal modes and late-time tails, *Phys. Rev. D* **102**, 044005 (2020).
- [33] J. P. Boyd, *Chebyshev and Fourier Spectral Methods*, Dover Books on Mathematics, 2nd ed. (Dover Publications, Mineola, NY, 2001).
- [34] S. I. Finazzo, R. Rougemont, M. Zaniboni, R. Critelli, and J. Noronha, Critical behavior of non-hydrodynamic quasinormal modes in a strongly coupled plasma, *J. High Energy Phys.* **01** (2017) 137.
- [35] P. A. González, E. Papantonopoulos, J. Saavedra, and Y. Vásquez, Superradiant Instability of Near Extremal and Extremal Four-Dimensional Charged Hairy Black Hole in anti-de Sitter Spacetime, *Phys. Rev. D* **95**, 064046 (2017).
- [36] P. A. Gonzalez, Y. Vasquez, and R. N. Villalobos, Perturbative and nonperturbative fermionic quasinormal modes of Einstein-Gauss-Bonnet-AdS black holes, *Phys. Rev. D* **98**, 064030 (2018).
- [37] R. Bécar, P. A. González, E. Papantonopoulos, and Y. Vásquez, Quasinormal modes of three-dimensional rotating Hořava AdS black hole and the approach to thermal equilibrium, *Eur. Phys. J. C* **80**, 600 (2020).
- [38] A. Aragón, R. Bécar, P. A. González, and Y. Vásquez, Perturbative and nonperturbative quasinormal modes of 4D Einstein-Gauss-Bonnet black holes, *Eur. Phys. J. C* **80**, 773 (2020).
- [39] R. A. Konoplya and M. S. Churilova, Non-evident stability of a Dirac field in Schwarzschild-de Sitter spacetime, [arXiv:2004.05879](https://arxiv.org/abs/2004.05879).
- [40] J. I. Jing, Dirac quasinormal modes of the Reissner-Nordström de Sitter black hole, *Phys. Rev. D* **69**, 084009 (2004).
- [41] J. F. Chang and Y. G. Shen, Massive quasinormal modes of a Schwarzschild-de Sitter black hole with a global monopole, *Int. J. Theor. Phys.* **45**, 2319 (2006).
- [42] A. Lopez-Ortega, Dirac quasinormal modes of D-dimensional de Sitter spacetime, *Gen. Relativ. Gravit.* **39**, 1011 (2007).
- [43] R. A. Konoplya and A. Zhidenko, Quasinormal modes of massive fermions in Kerr spacetime: Long-lived modes and the fine structure, *Phys. Rev. D* **97**, 084034 (2018).
- [44] H. T. Cho, Dirac quasinormal modes in Schwarzschild black hole space-times, *Phys. Rev. D* **68**, 024003 (2003).
- [45] D. P. Du, B. Wang, and R. K. Su, Quasinormal modes in pure de Sitter space-times, *Phys. Rev. D* **70**, 064024 (2004).
- [46] Wolfram *Mathematica* 10, <http://www.wolfram.com>, 2015.
- [47] B. Mashhoon, Quasi-normal modes of a black hole, in Third Marcel Grossmann Meeting on General Relativity, 1983.
- [48] B. F. Schutz and C. M. Will, Black hole normal modes: A semianalytic approach, *Astrophys. J. Lett.* **291**, L33 (1985).
- [49] S. Iyer and C. M. Will, Black hole normal modes: A WKB approach. 1. Foundations and application of a higher order WKB analysis of potential barrier scattering, *Phys. Rev. D* **35**, 3621 (1987).
- [50] R. A. Konoplya, Quasinormal behavior of the d-dimensional Schwarzschild black hole and higher order WKB approach, *Phys. Rev. D* **68**, 024018 (2003).
- [51] J. Matyjasek and M. Opala, Quasinormal modes of black holes. The improved semianalytic approach, *Phys. Rev. D* **96**, 024011 (2017).
- [52] R. A. Konoplya, A. Zhidenko, and A. F. Zinhailo, Higher order WKB formula for quasinormal modes and grey-body factors: Recipes for quick and accurate calculations, *Classical Quantum Gravity* **36**, 155002 (2019).
- [53] Y. Hatsuda, Quasinormal modes of black holes and Borel summation, *Phys. Rev. D* **101**, 024008 (2020).